

# First-Principles Study of CO Adsorption and Vibration on Au Surfaces

D. Loffreda\* and P. Sautet

Laboratoire de Chimie, UMR CNRS 5182, Ecole Normale Supérieure de Lyon,  
46 Allée d'Italie F-69364 Lyon Cedex 07, France

Received: January 27, 2005; In Final Form: March 15, 2005

A CO stretching frequency analysis is presented for the adsorption of CO on various Au(110) surfaces from density functional theory calculations. The structure sensitivity of the adsorption has been studied by considering the unreconstructed ( $1 \times 1$ ) surface, the missing-row reconstructed ( $1 \times 2$ ) surface, the vicinal stepped ( $\bar{2}30$ ) surface, and the adsorption on adatoms deposited on the (110)-( $1 \times 2$ ) surface. The calculated CO stretching frequencies are compared with infrared reflection–absorption spectroscopy (IRAS) measurements carried out at room temperature and pressure below 1 atm. The overall stability of the systems is discussed within the calculations of surface free energies at various coverages. At room temperature, the adsorption of CO on the ridge of the missing-row reconstructed surface competes in the high pressure regime with more complex adsorption structures where the molecule coadsorbs on the ridge and on adatoms located along the empty troughs of the reconstruction. This result is supported by the CO stretching frequency analysis.

## I. Introduction

Catalysis by gold has been the subject of numerous experimental studies over the last 10 years.<sup>1–3</sup> This noble metal, which has been usually known as a relatively inert catalyst, has recently shown an interesting catalytic behavior toward CO oxidation when gold particles are deposited on various oxide supports.<sup>4,5</sup> This unexpected activity in a dispersed form at low temperature could have an important impact in the future design of fuel cells, in particular for the removal of CO from the hydrogen gas fuel.<sup>6–8</sup> Recent efforts have been developed to study CO adsorption on Au(110) in the high pressure and high temperature environment.<sup>9</sup> According to high pressure scanning tunneling microscopy (STM) observations, CO adsorption is also possible on this inert surface in the high pressure range.

The clean Au(110) surface exhibits a well-known ( $1 \times 2$ ) missing-row reconstruction at room temperature, where every second  $[\bar{1}10]$  row of atoms is absent. This surface has been investigated extensively by classical STM during the last two decades<sup>10–14</sup> and also more recently by in situ STM<sup>15,16</sup> at higher temperatures. The high temperature STM results show that the missing-row reconstruction is stable up to 700 K.<sup>16</sup> This surface undergoes two phase transitions upon heating: an Ising transition at 650 K in which the surface deconstructs and a 3D roughening transition at 700 K. The authors conclude that ( $1 \times 3$ ) steps of Au(110) parallel to  $[\bar{1}10]$  are also stable up to 500 K.

Since early ultrahigh vacuum (UHV) measurements have shown that the heat of adsorption of CO on Au(110) is weak at low temperature ( $33\text{--}67\text{ kJ}\cdot\text{mol}^{-1}$ ),<sup>17</sup> only a few studies have been devoted to CO adsorption on gold single-crystal surfaces. Indeed, many of the reports have been dedicated to the investigation of CO adsorption on supported gold particles and on polycrystalline gold. However, Ruggiero et al. have reported an extensive low energy electron diffraction (LEED), thermal desorption spectroscopy (TDS), and reflection–absorption

infrared spectroscopy (RAIRS) study of CO adsorption on Au-(332) at 92 and 105 K.<sup>18,19</sup> They have estimated an initial isosteric heat of adsorption of  $55\text{ kJ}\cdot\text{mol}^{-1}$  for this surface. More recently, Gottfried et al. have published a combined TDS, ultraviolet photoemission spectroscopy (UPS), work function measurement (DF), LEED, and near edge X-ray absorption fine structure (NEXAFS) study concerning CO adsorption on Au-(110)-( $1 \times 2$ ) under UHV conditions at temperatures between 28 and 300 K.<sup>20</sup> The authors have shown that CO adsorption is molecular below 150 K with a high initial sticking probability of 0.9 at 28 K. An isosteric heat of adsorption of  $59\text{ kJ}\cdot\text{mol}^{-1}$  ( $0.61\text{ eV}$ ) at zero coverage limit has corroborated the previous result on Au(332). On Au(110)-( $1 \times 2$ ), Gottfried et al. predict from a Clausius–Clapeyron model that CO adsorption is nonactivated on gold and that CO is weakly chemisorbed for coverages below 0.5 ML (ML = monolayer) and physisorbed for coverages between 0.5 and 1.0 ML. Thermal desorption spectra corresponding to initial coverage  $\leq 1$  ML show three peaks at 55 ( $\gamma$ -CO), 67 ( $\delta$ -CO), and 145 K ( $\epsilon$ -CO) which have been attributed to the desorption of the molecules in direct contact with the surface. On the basis of TDS measurements with an initial coverage of 2.9 ML, the so-called  $\delta$ -CO and  $\epsilon$ -CO desorption states have been assigned to coexistent physisorbed and chemisorbed CO, respectively, and associated with desorption activation energies ranging from  $18.5 \pm 1.3$  to  $38.4 \pm 2.8\text{ kJ}\cdot\text{mol}^{-1}$ . In the whole coverage and temperature range, the authors have not observed any ordered CO overlayer structures.<sup>20</sup>

The classical surface science techniques customarily used for investigating heterogeneous catalytic systems are limited at pressures much lower than the environments of working technical catalysts. This well-known limitation usually called “pressure gap” prevents direct comparisons between model and industrial catalysts.<sup>21,22</sup> However, the recent development of in situ surface sensitive techniques designed for operating under an elevated pressure environment, such as STM,<sup>23</sup> sum frequency generation (SFG),<sup>24</sup> and polarized modulation infrared reflection–absorption spectroscopy (PM-IRAS),<sup>25</sup> is now open-

\* Corresponding author. E-mail: David.Loffreda@ens-lyon.fr. Homepage: <http://perso.ens-lyon.fr/david.loffreda>.

ing new horizons in particular when high pressure is required to reach measurable adsorption coverages. Recently, Y. Jugnet et al. have reported the first results of a direct experimental observation of CO chemisorption on Au(110) at 300 K by polarized RAIRS and STM, both techniques operated under a CO pressure ranging from UHV up to hundreds of Torr.<sup>9</sup> In the range  $10^{-1}$ – $10^2$  Torr, RAIRS measurements have revealed a CO chemisorption with a stretching frequency of  $2110\text{ cm}^{-1}$  assigned to on top adsorbed CO. The intensity of the band increases with the pressure until saturation occurring at about 10 Torr. No significant wavenumber shift or bandwidth modification has been observed. Under a pressure of 100 Torr, a new band has appeared at  $2141\text{ cm}^{-1}$  close to the CO gas-phase value ( $2143\text{ cm}^{-1}$ ). STM images under UHV up to  $10^{-5}$  Torr have shown the missing-row reconstruction at 300 K. At higher CO pressure, a deep restructuring of the surface has been observed in the range 1–500 Torr. The lifting of the anisotropy of the terraces has been assigned to a transition from a  $(1 \times 2)$  to a  $(1 \times 1)$  surface atomic arrangement. More recently, IRAS measurements on Au(110)- $(1 \times 2)$ , operated in the  $10^{-8}$ – $10^{-4}$  Torr pressure range varying the sample temperature, have shown a red shift of the stretching frequency from 2118 to  $2108\text{ cm}^{-1}$ , when the temperature decreases from 170 to 110 K.<sup>26</sup>

From a theoretical point of view, a few studies have been devoted to the investigation of CO adsorption on gold surfaces. All the published studies based on density functional theory (DFT) report on CO adsorption on vicinal Au(110)<sup>27</sup> and Au(111) surfaces,<sup>28–31</sup> and recently also on Au particles supported by MgO(100).<sup>32,33</sup> However, no theoretical work has been published up to now for CO on Au(110)- $(1 \times 2)$ , although the adsorption at the edge of Au particles reported previously is similar to the ridge termination considered in the present work. For CO on Au(110)- $(1 \times 1)$ , Perdew–Wang 91 generalized gradient approximation (PW91-GGA) results show that the adsorption on a top site ( $-0.69\text{ eV}$ ) is slightly more stable than the one on a short bridge site ( $-0.67\text{ eV}$ ) for a coverage of 0.25 ML.<sup>27</sup> The calculated stretching frequencies are respectively 2042 and  $1962\text{ cm}^{-1}$  for top and short bridge adsorptions. For CO on Au(111), the adsorption energy calculated at the PW91-GGA level is ranging from  $-0.04$ <sup>28</sup> to  $-0.30\text{ eV}$ <sup>29</sup> for top adsorption in a  $(2 \times 2)$  unit cell (coverage  $1/4\text{ ML}$ ). Conversely, other authors have found more recently a favored face-centered cubic (fcc) hollow adsorption with an adsorption energy ranging from  $-0.17$ <sup>30</sup> to  $-0.40\text{ eV}$ <sup>31</sup> for the same coverage at the Perdew–Burke–Ernzerhof (PBE) and PW91-GGA levels, respectively. Different adsorption energy results have also been reported for CO on Au(211). Mavrikakis et al. have calculated a value of  $-0.66\text{ eV}$  for a bridge site at a coverage of  $1/6\text{ ML}$ ,<sup>29</sup> whereas Liu et al. have found  $-1.05\text{ eV}$  for the same site and coverage.<sup>30</sup> According to the computational details given in these studies, we infer that the adsorption energies on gold seem to be very sensitive to the density of k-point sampling and that the range of published values results from a not fully complete convergence on this aspect. For top CO adsorption at the edge of Au particles supported on MgO(100), Molina et al. have found a chemisorption energy of  $-0.72$  and  $-0.41\text{ eV}$  with PW91 and revised PBE-GGA functionals, respectively.<sup>33</sup>

Despite recent experimental efforts, the restructuring mechanism from Au(110)- $(1 \times 2)$  to Au(110)- $(1 \times 1)$  induced by elevated CO pressure is not understood yet. At room temperature and high pressure, this transition or even a change of coverage does not seem to be accompanied by a vibrational shift of the CO stretching frequency. Conversely, a red shift is observed at lower temperature and pressure when the coverage increases.

Hence, the dependence of the CO vibrations on the Au(110) surface with the temperature and pressure conditions has to be elucidated.

In this work, we report DFT-GGA results for the modeling of CO adsorption on both missing-row and unreconstructed Au(110) surfaces and also on the vicinal Au(230) stepped surface at various coverages. Efforts have been made to compare the stability of all the considered surfaces as a function of temperature and CO gas pressure. An equilibrium-thermodynamical model based on GGA total energies has been applied to predict the stability of a phase (site and coverage) in the range of the experimental results. The thermodynamics of CO on Au(110) has been studied by a systematic CO stretching frequency analysis at least for the most stable sites. Thus, total energy calculations combined with CO vibration analysis are presented and compared with experimental TDS and RAIRS observations.

## II. Methodology

The geometry optimizations and the C–O stretching vibrations have been performed using the Vienna ab initio simulation program (VASP).<sup>34,35</sup> The Kohn–Sham equations are solved with the generalized gradient approximation (GGA) proposed by Perdew and Wang.<sup>36</sup> The projector-augmented-wave (PAW) method of Blöchl,<sup>37</sup> in the formulation of Kresse and Joubert,<sup>38</sup> is applied to describe electron–ion interactions. This method, being essentially all electron, improves not only the description of transition metals compared to the use of pseudopotentials but also, in our case, the description of the Au–CO electronic interactions. Brillouin-zone sampling is performed on Monkhorst–Pack special points<sup>39</sup> using a Methfessel–Paxton integration scheme. The plane-wave cutoff is set to 400 eV throughout all calculations. Sufficient convergence with respect to energy cutoff has been confirmed.

The surfaces are modeled by slabs containing six atomic Au layers with a CO molecule adsorbed only on one side of the slab. Symmetrized slabs of 11 layers have also been considered, showing negligible differences for adsorption energies and optimized geometries. The optimized bulk nearest neighbor separation has been chosen in all our calculations ( $2.95\text{ Å}$ ). The vacuum separation between periodically repeated slabs corresponds to seven bulk equivalent layers ( $8.9\text{ Å}$ ). In the geometry optimization procedure, the freedom degrees of the CO molecule and the four uppermost Au layers are relaxed, while the two lowest metallic planes are frozen in a bulklike geometry.

Various adsorption structures and coverages have been considered (cf. Figure 1). For a given surface  $i$  with a unit cell area  $A_i$  containing  $N_{\text{CO}}$  CO molecules, the coverage (%) is defined as the molecule density normalized to the smallest unit cell area  $A_{1 \times 1}$  of Au(110)- $(1 \times 1)$ :

$$\theta = N_{\text{CO}}/A_i \times A_{1 \times 1} \quad (1)$$

For Au(110)- $(1 \times 1)$ , five different coverages have been explored:  $(1 \times 1)$  100%,  $(2 \times 1)$ ,  $(1 \times 2)$ , or  $c(2 \times 2)$  50%,  $(2 \times 2)$  25%,  $(3 \times 2)$  16.67%, and  $(4 \times 2)$  12.5%. For Au(110)- $(1 \times 2)$ , four different coverages have been explored:  $(1 \times 1)$  50%,  $(2 \times 1)$  25%,  $(3 \times 1)$  16.67%, and  $(4 \times 1)$  12.5%. The coadsorption on the Au adatoms present along the empty missing rows and on the ridges of Au(110)- $(1 \times 2)$  has also been modeled with two different supercells:  $(2 \times 1)$  (75, 50, and 25%) and  $(3 \times 1)$  (66.67, 50, 33.33, and 16.67%). According to our coverage definition, the saturation coverage corresponds to 100% (one monolayer) on Au(110)- $(1 \times 1)$  and to 50% on Au(110)- $(1 \times 2)$ . Adsorption on steps is reported on the vicinal

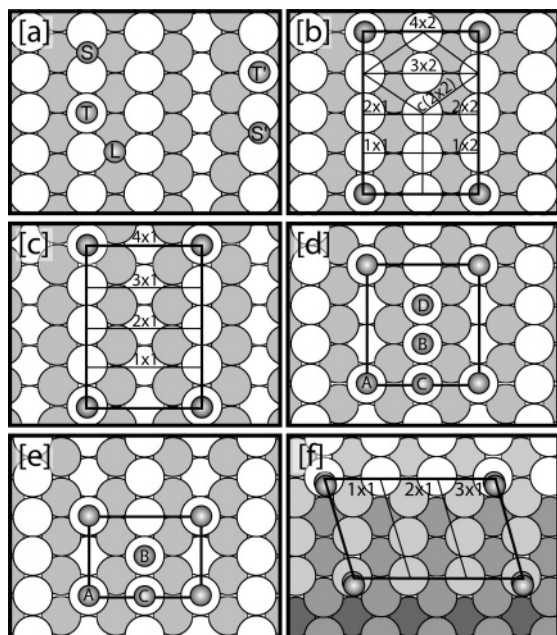


**Figure 1.** Top views of the CO adsorption on various Au surfaces. (a) The stable adsorption sites are reported for the Au(110)-(1 × 1) surface (T = top, S = short bridge, L = long bridge) and for the Au(110)-(1 × 2) surface (T' = top, S' = short bridge). The considered adsorption unit cells are presented (b) on Au(110)-(1 × 1), (c) on Au(110)-(1 × 2), on Au(110)-(1 × 2) presenting a gold adatom in the missing row with (d) a (3 × 1) or (e) a (2 × 1) periodicity and (f) on Au(230). For parts d and e, the coverage increases with the number of CO molecules adsorbed in the unit cell. In part d, A corresponds to (3 × 1)-1CO (16.67%), A + B to (3 × 1)-2CO (33.33%), A + B + C to (3 × 1)-3CO (50%), and A + B + C + D to (3 × 1)-4CO (66.67%). In part e, A corresponds to (2 × 1)-1CO (25%), A + B to (2 × 1)-2CO (50%), and A + B + C to (2 × 1)-3CO (75%).

Au(230) surface with the following coverages: (1 × 1) 39.25%, (2 × 1) 19.63%, and (3 × 1) 13.08%. In this case, the coverage is changed along the step where the adsorption is preferential. Five different adsorption sites have been optimized (cf. Figure 1): top for all surfaces, short bridge for Au(110)-(1 × 1) and (1 × 2) surfaces, long bridge for Au(110)-(1 × 1) and Au(230), 4-fold hollow for Au(110)-(1 × 1), and 3-fold pseudohollow for Au(110)-(1 × 2). The top site is always the most stable one whatever the surface or the coverage. The 4-fold hollow and 3-fold pseudohollow sites are not local minima on the potential energy surface.

Vertically adsorbed CO has a significant dipole moment. The errors caused by the periodic lattice of dipoles<sup>40</sup> have been corrected by adding a linear electrostatic potential to the local potential (a saw-tooth-shaped potential to verify the periodicity constraints<sup>41</sup>). The anharmonic stretching frequency calculation technique is based on the numerical calculation of the second derivatives of the potential energy surface. For all the surfaces and adsorption structures, the vibrational treatment is simplified by neglecting the weak coupling between the C–O stretching and the metallic phonon. When only one stretching frequency is calculated (one CO molecule in the unit cell), the coupling between the CO stretching, the bending vibrations, and the frustrated translations is neglected for the same reasons. In this case, the gold slab is fixed to the optimized geometry of the considered chemisorption structure, and the C–O bonds are stretched, with the center of mass of the molecule being fixed. The potential energy curves are fitted with Morse-shape potential, developed at the third order around the equilibrium state. A good accuracy for the fit of the potential is reached

with a sampling of 11 equidistant calculated points in the range of ±0.05 Å around the equilibrium C–O distance. Moreover, the quality of the fit has been improved by increasing the size of the basis set with a higher energy cutoff (500 eV). The anharmonic stretching frequency can be directly computed from the potential constants. The exact expression of the anharmonic stretching frequency ( $\nu_{\text{an}}$ ) can be divided into a simple harmonic frequency ( $\nu_{\text{ha}}$ ) and a second term which corresponds to the corrective anharmonic frequency ( $\nu_{\text{c}}$ ).<sup>42</sup> The numeric error in the anharmonic frequency calculation is estimated to 8 cm<sup>-1</sup> by fitting the potential with fourth-order developments of the Morse potential. Thus, third-order equations provide a good accuracy. The average value for the corrective anharmonic frequencies is 27 cm<sup>-1</sup>. When more than one stretching frequency is calculated (more than one CO molecule in the unit cell), the vibrational analysis is performed only at the harmonic level with the numerical calculation and diagonalization of the Hessian matrix (force constant matrix) by considering all the freedom degrees of the CO molecules.

Atomistic thermodynamics is linked to first-principle calculations in order to determine the stability of the adsorbed system under the high pressure and temperature conditions. The appropriate thermodynamic potential is the surface free energy ( $\gamma_{\text{surf}}$ ) which is the result of a balance between the energetic loss due to the formation of the surface from the bulk and the energetic gain due to the adsorption.  $\gamma_{\text{surf}}$  is calculated as the difference between the total Gibbs free energy ( $G_{\text{tot}}$ ) of the chemisorbed system and the chemical potentials of the Au bulk ( $\mu_{\text{Au}}^{\text{bulk}}$ ) and the gas-phase ( $\mu_{\text{CO}}^{\text{gas}}$ ) references, as<sup>43–45</sup>

$$\gamma_{\text{surf}}^{\theta}(T, P) = \frac{1}{A}(G_{\text{tot}}^{\theta} - N_{\text{Au}}\mu_{\text{Au}}^{\text{bulk}} - N_{\text{CO}}\mu_{\text{CO}}^{\text{gas}}) \quad (2)$$

where  $N_{\text{Au}}$  and  $N_{\text{CO}}$  are the respective total numbers of Au atoms and CO molecules in the unit cell of area  $A$ . In the model, the CO gas phase plays the role of a reservoir which imposes its temperature ( $T$ ) and pressure ( $P$ ) to the adsorbed phase. The vibrational energy and entropy contributions to the Gibbs free energy should be calculated in principle. However, since the weak CO adsorption does not modify strongly the adsorbate vibrations and substrate phonons, these contributions can be neglected.<sup>46</sup> Hence,  $G_{\text{tot}}^{\theta}$  and  $\mu_{\text{Au}}^{\text{bulk}}$  are approximated as DFT total energies ( $E_{\text{tot}}^{\theta}$  and  $E_{\text{Au}}^{\text{bulk}}$ , respectively). Within these simplifications, the surface free energy ( $\gamma_{\text{surf}}^{\theta}(T, P)$ ) reads (cf. eq 3):

$$A \times \gamma_{\text{surf}}^{\theta}(T, P) \approx E_{\text{tot}}^{\theta} - N_{\text{Au}}E_{\text{Au}}^{\text{bulk}} - N_{\text{CO}}E_{\text{CO}}^{\text{gas}} - 5N_{\text{CO}}kT/2 + N_{\text{CO}}kT \ln(Z_{\text{CO}}^{\text{trans}}(T, P) Z_{\text{CO}}^{\text{rot}}(T)) - N_{\text{CO}}kT \ln(P/P_0) \quad (3)$$

where  $A$  is the area of the unit cell.  $E_{\text{tot}}^{\theta}$ ,  $E_{\text{Au}}^{\text{bulk}}$ , and  $E_{\text{CO}}^{\text{gas}}$  are the DFT total energies for the adsorbed phase, the bulk phase, and the CO gas phase, respectively. The internal translational ( $3/2kT$ ) and rotational ( $kT$ ) energies are included for the gas phase. The total entropy change during the adsorption process depends explicitly only on the translational ( $Z_{\text{CO}}^{\text{trans}}(T, P)$ ) and rotational ( $Z_{\text{CO}}^{\text{rot}}(T)$ ) partition functions of the gas phase, since the vibrational partition function contributions of the adsorbed system, the clean surface (or bulk), and the gas phase have been simplified in a first approximation. The last term  $kT \ln(P/P_0)$  comes from the temperature and pressure dependence of the gas-phase chemical potential.

There are two main sources of errors for the calculations of total energies and adsorption energies. The “numerical” error is related to the convergence of these energies with calculation



**TABLE 1: Clean Au(110)-(1 × 1) and Missing-Row Au(110)-(1 × 2) Surfaces—Surface Energy ( $\sigma_{\text{surf}}$ , meV·Å<sup>-2</sup>) at Zero Temperature and Optimized Geometry<sup>a</sup>**

	this work		theoretical calculations						experimental results			
	DFT		DFT	SARIS <sup>47</sup>	FP <sup>48</sup>	MEAM <sup>49</sup>	SC <sup>50</sup>	MM <sup>51</sup>	LEED <sup>11</sup>	LEIS <sup>52</sup>	MEIS <sup>53</sup>	XRD <sup>54</sup>
	(1 × 1)	(1 × 2)	(1 × 2)	(1 × 2)	(1 × 2)	(1 × 2)	(1 × 2)	(1 × 2)	(1 × 2)	(1 × 2)	(1 × 2)	(1 × 2)
$\Delta d_{12}$ (%)	-0.21	-0.34		-0.25	-0.23	-0.31	-0.16	-0.09	-0.29	-0.20	-0.26	-0.32 ± 0.1
$\Delta d_{23}$ (%)	+0.13	+0.04		+0.10	+0.03	-0.07	-0.05	-0.03	+0.03		+0.06	
$\Delta d_{34}$ (%)	-0.06	-0.02		-0.01		-0.38			-0.09			
$\Delta d_{45}$ (%)	+0.03	+0.03		+0.01								
$\Delta d_{56}$ (%)	(0)	(0)										
$b_3$ (Å)		+0.32		+0.12	+0.20	+1.04	+0.10	+0.05	+0.24		+0.20	
$b_{3'}$ (Å)		-0.17							-0.09			
$b_{3''}$ (Å)		+0.15							+0.15			
$p_2$ (Å)	0	0.05		0.01	0.05	0.01	-0.03	0.02	0.07	<0.1	<0.1	0.05 ± 0.01
$p_4$ (Å)	0	0.07		0.02	0.09				0.003			0.05 ± 0.01
$\sigma_{\text{surf}}$	109.9	101.3	82 <sup>55</sup> 91 <sup>56</sup>			61.8		97.4				

<sup>a</sup> The geometric parameters are the ones defined in Figure 2.  $\Delta d_{ij}$  parameters are calculated as a percentage of the ideal bulk interplane spacing.

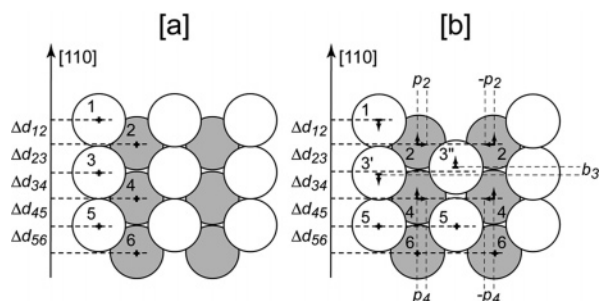


**Figure 2.** Schematic lateral views of (a) the bare Au(110)-(1 × 1) and (b) the missing-row Au(110)-(1 × 2) surfaces. All the geometric parameters reported in Tables 1 and 2 are defined.

parameters such as the k-point densities or the size of the plane-wave basis set. Special care has been taken in the total energy convergence with k-point sampling to ensure a tight convergence of  $\gamma_{\text{surf}}$  ( $\leq 1$  meV·Å<sup>-2</sup>).<sup>58</sup> The error due to the basis set is less than 2.5 meV·Å<sup>-2</sup> for the surface free energy. It has been estimated by increasing the energy cutoff up to 500 eV (highly accurate calculations). The “systematic” error of the model, which is related to the supercell approach, has been calculated by considering thicker metallic slabs (up to eight Au layers). The error in the surface free energy associated to the choice of a six-layer slab is less than 1 meV·Å<sup>-2</sup>. Our value is smaller than the one published previously ( $\pm 5$  meV·Å<sup>-2</sup>).<sup>45,46</sup> The configurational entropy contribution to the surface free energy is found negligible in the considered temperature range (below 1 meV·Å<sup>-2</sup>).

### III. DFT Calculations

**A. Clean Surfaces.** The geometry optimizations of the bare Au(110)-(1 × 1) and missing-row Au(110)-(1 × 2) surfaces are presented in Table 1 and in Figure 2.

The surface energy ( $\sigma_{\text{surf}}$ ) at zero temperature is calculated as follows:

$$\sigma_{\text{surf}} = \frac{E_{\text{tot}}^{1 \times 1, 1 \times 2} - N_{\text{Au}} E_{\text{Au}}^{\text{bulk}}}{2A_{1 \times 1, 1 \times 2}} \quad (4)$$

$\sigma_{\text{surf}}$  is calculated with symmetrized slabs of 11 layers. The missing-row (1 × 2) surface has a lower surface energy (101.3 meV·Å<sup>-2</sup>) than the (1 × 1) one (109.9 meV·Å<sup>-2</sup>), as shown previously in refs 55 and 56 and references therein (cf. Table 1 for details). The geometry optimization of the (1 × 2) surface

yields a good agreement with LEED.<sup>11</sup> The first interlayer spacing ( $\Delta d_{12}$ ) shows a small contraction (−0.34%) in agreement with LEED<sup>11</sup> but also XRD.<sup>54</sup> The optimized buckling ( $b_3$ ) agrees also with the LEED model, in contrast with previous theoretical models. The lower other interlayer spacings show a more moderate relaxation. The (1 × 1) surface is characterized by a smaller contraction of the first interlayer spacing (−0.21%) and a larger expansion of the second one compared to the (1 × 2) surface.

**B. Adsorption from Atomistic Thermodynamics.** Various adsorption sites have been considered on the Au(110) surfaces for the saturation coverage (100% for (1 × 1) and 50% for (1 × 2)) and for a lower coverage (25%). The optimized geometries of the stable adsorption forms are summarized in Table 2 and presented in Figure 1a.

For the (1 × 1) surface at saturation coverage, the top site is the most stable site (−0.56 eV). The adsorption process induces a stronger contraction of the first interlayer spacing (−8.2%) than the one reported for the bare surface. More surprising is the small contraction (−0.6%) of the second interlayer spacing compared to the small expansion noticed in the case of the clean surface (+0.13%). The optimized CO distance is slightly longer (1.154 Å) than the one calculated in the gas phase (1.142 Å). The short bridge site, which is less stable than the top one (−0.39 eV), shows in contrast an expansion of the first interlayer spacing (+1.3%) and a longer CO bond length (1.169 Å). The least competitive site is the long CO bridge one (−0.05 eV) where the molecule is located far from the Au surface (2.153 Å). In this latter case, the expansion of the first interlayer spacing is even larger (+5%). At a lower coverage of 25%, the top and the short bridge sites have a similar stability (−0.62(3) and −0.61(7) eV, respectively). The contraction of the first interlayer spacing increases up to −12.1%. In contrast with the saturation coverage, there is an expansion of the second interlayer spacing (+6.7%). For the (1 × 2) surface at a coverage of 50%, the top site is also the preferential adsorption form (−0.52 eV). The contraction of the first interlayer spacing (−7.9%) is equivalent to the top site on Au(110)-(1 × 1). This contraction is also significant in this case for the second interlayer spacing (−4.3%). At a lower coverage of 25%, the top site is also the preferential adsorption form (−0.69 eV). The calculated contraction of the first interlayer spacing is twice stronger in this case (−16.6%). As a summary, the top site is the most stable one for the Au(110) surfaces. For the adsorption on the steps of Au(230), the top site is also preferential.

**TABLE 2: Adsorption Energy ( $E_{\text{ads}}$ ), Anharmonic C–O Stretching Frequency ( $\nu_{\text{an}}$ ), and Optimized Geometry of the Stable CO Adsorption Sites on Au(110)-(1  $\times$  1) and Au(110)-(1  $\times$  2) Surfaces, Reported in Figure 1<sup>a</sup>**

	(1 $\times$ 1)					(1 $\times$ 2)				gas phase	
	T	S	L	T	S	T'	S'	T'	S'	this work	expt
coverage (%)	100	100	100	25	25	50	50	25	25		
$E_{\text{ads}}$ (eV)	−0.56	−0.39	−0.05	−0.62(3)	−0.61(7)	−0.52	−0.35	−0.69	−0.58		
$\nu_{\text{an}}$ (cm <sup>−1</sup> )	2081	1916	1971	2039	1886	2030	1933	2044	1893	2106	2143
$d(\text{C–O})$ (Å)	1.154	1.169	1.158	1.151	1.170	1.155	1.170	1.151	1.168	1.142	1.128
$d(\text{Au–C})$ (Å)	1.995	2.102	2.513	1.986	2.084	2.029	2.116	2.000	2.115		
$\Delta d_{12}$ (%)	−8.2	+1.3	+5.0	−12.1	−8.2	−7.9	+0.6	−16.6	−7.2		
$\Delta d_{23}$ (%)	−0.6	−2.6	−2.6	+6.7	+6.9	−4.3	−5.5	−0.5	−3.0		
$\Delta d_{34}$ (%)	+1.7	+1.8	+1.2	−2.7	−2.9	+4.4	+4.3	+2.1	+2.6		
$\Delta d_{45}$ (%)	−1.7	−2.2	−1.0	+2.0	+2.2	−1.0	−1.0	+0.5	+0.6		
$\Delta d_{56}$ (%)	(0)	(0)	(0)	(0)	(0)	(0)	(0)	(0)	(0)		
$b_{3'}$ (Å)						+0.010	−0.08	−0.11	−0.12		
$b_{3''}$ (Å)						+0.012	+0.08	+0.11	+0.12		
$p_2$ (Å)	0	0	0	0	0	+0.04	+0.01	+0.05	+0.03/−0.004		
$p_4$ (Å)	0	0	0	0	0	+0.03	+0.03	+0.04	+0.05/+0.04		

<sup>a</sup> The geometric parameters are the ones defined in Figure 2.  $\Delta d_{ij}$  parameters are calculated as a percentage of the ideal bulk interplane spacing. The definitions of the sites T, S, L, T', and S' are given in Figure 1a.

**TABLE 3: Adsorption Energy ( $E_{\text{ads}}$ ) and Scaled Harmonic ( $\tilde{\nu}_{\text{ha}}$ ) and Anharmonic ( $\tilde{\nu}_{\text{an}}$ ) C–O Stretching Frequency of the Top Site on the Au(110)-(1  $\times$  1) Surface as a Function of Coverage<sup>a</sup>**

Au(110)-(1 $\times$ 1)	(4 $\times$ 2)	(3 $\times$ 2)	(2 $\times$ 2)	(1 $\times$ 2)	(1 $\times$ 1)
coverage (%)	12.5	16.67	25	50	100
$E_{\text{ads}}$ (eV)	−0.66	−0.65	−0.62	−0.69	−0.56
$d(\text{C–O})$ (Å)	1.150	1.150	1.151	1.153	1.154
$\tilde{\nu}_{\text{ha}}$ (cm <sup>−1</sup> )	2102	2106	2101	2103	2116
$\tilde{\nu}_{\text{an}}$ (cm <sup>−1</sup> )	2075	2076	2075	2079	2092
$\Delta\tilde{\nu}_{\text{ha}}$ (cm <sup>−1</sup> )	−34	−30	−35	−33	−20
$\Delta\tilde{\nu}_{\text{an}}$ (cm <sup>−1</sup> )	−34	−33	−33	−30	−17

<sup>a</sup> The harmonic or anharmonic scaling factor is 1.017. The harmonic ( $\Delta\tilde{\nu}_{\text{ha}}$ ) and anharmonic ( $\Delta\tilde{\nu}_{\text{an}}$ ) frequency variation differences are defined in eq 5.

**TABLE 4: Adsorption Energy ( $E_{\text{ads}}$ ) and Scaled Harmonic ( $\tilde{\nu}_{\text{ha}}$ ) and Anharmonic ( $\tilde{\nu}_{\text{an}}$ ) C–O Stretching Frequency of the Top Site on the Au(110)-(1  $\times$  2) Surface as a Function of Coverage<sup>a</sup>**

Au(110)-(1 $\times$ 2)	(4 $\times$ 1)	(3 $\times$ 1)	(2 $\times$ 1)	(1 $\times$ 1)	(3 $\times$ 1)-Ad	(2 $\times$ 1)-Ad
coverage (%)	12.5	16.67	25	50	16.67	25
$E_{\text{ads}}$ (eV)	−0.69	−0.73	−0.69	−0.52	−0.91	−0.91
$d(\text{C–O})$ (Å)	1.150	1.150	1.151	1.153	1.150	1.151
$\tilde{\nu}_{\text{ha}}$ (cm <sup>−1</sup> )	2100	2095	2096	2100	2105	2099
$\tilde{\nu}_{\text{an}}$ (cm <sup>−1</sup> )	2073	2070	2072	2079	2079	2075
$\Delta\tilde{\nu}_{\text{ha}}$ (cm <sup>−1</sup> )	−36	−41	−40	−36	−31	−37
$\Delta\tilde{\nu}_{\text{an}}$ (cm <sup>−1</sup> )	−35	−39	−36	−30	−30	−33

<sup>a</sup> The harmonic or anharmonic scaling factor is 1.017. The harmonic ( $\Delta\tilde{\nu}_{\text{ha}}$ ) and anharmonic ( $\Delta\tilde{\nu}_{\text{an}}$ ) frequency variation differences are defined in eq 5.

On the (1  $\times$  1) surface, the adsorption becomes stronger (from 0.56 to 0.62–0.69 eV) when the coverage decreases from saturation (100%) to low coverages (12.5%) (cf. Table 3).

The trend is similar for the (1  $\times$  2) surface with a slightly stronger variation (from 0.52 to 0.69–0.73 eV), as shown in Table 4. The DFT results agree qualitatively with recent thermal desorption spectroscopy observations on Au(110)-(1  $\times$  2)<sup>20</sup> where a lowering of the adsorption energy is reported from 0.61 eV (at zero coverage limit) to 0.36 eV (at 0.45 ML). A qualitative agreement is also obtained with Clausius–Clapeyron data analysis yielding a more moderate variation of the CO adsorption heat (from 0.47 to 0.34 eV).<sup>26</sup> As shown previously for CO adsorption on various metallic surfaces,<sup>57</sup> the PW91-GGA functional generally overestimates the chemisorption energies (0.1 eV in our case at zero coverage limit). On the

**TABLE 5: Adsorption Energy ( $E_{\text{ads}}$ ) and Scaled Harmonic ( $\tilde{\nu}_{\text{ha}}$ ) and Anharmonic ( $\tilde{\nu}_{\text{an}}$ ) C–O Stretching Frequency of the Top Site on the Au(230) Surface as a Function of Coverage<sup>a</sup>**

Au(230)	(3 $\times$ 1)	(2 $\times$ 1)	(1 $\times$ 1)
coverage (%)	13.08	19.63	39.25
$E_{\text{ads}}$ (eV)	−0.73	−0.72	−0.70
$d(\text{C–O})$ (Å)	1.150	1.150	1.150
$\tilde{\nu}_{\text{ha}}$ (cm <sup>−1</sup> )	2103	2102	2103
$\tilde{\nu}_{\text{an}}$ (cm <sup>−1</sup> )	2077	2077	2077
$\Delta\tilde{\nu}_{\text{ha}}$ (cm <sup>−1</sup> )	−33	−34	−33
$\Delta\tilde{\nu}_{\text{an}}$ (cm <sup>−1</sup> )	−32	−32	−32

<sup>a</sup> The harmonic or anharmonic scaling factor is 1.017. The harmonic ( $\Delta\tilde{\nu}_{\text{ha}}$ ) and anharmonic ( $\Delta\tilde{\nu}_{\text{an}}$ ) frequency variation differences are defined in eq 5.

surface defects, the chemisorption is enhanced with a strongest interaction on Au adatoms (−0.91 eV) at low coverages (16.67 and 25%). On the steps of Au(230), the top site is also more stable than on the flat Au(110) surfaces with an adsorption energy of 0.70–0.73 eV depending on the coverage along the step (cf. Table 5).

For each considered surface and adsorption structure, the surface free energy curves are plotted for two different pressures and temperatures (cf. Figure 3). For a fixed low pressure of 10<sup>−8</sup> Torr and in the range 100–200 K of temperatures (cf. Figure 3a), different adsorption structures are in competition: the missing-row Au(110)-(1  $\times$  2) surface at a low coverage (16.7%) and the same surface presenting one Au–CO in the empty trough with a low density (16.7%). According to the absolute positions of the corresponding clean surfaces, the adsorption should be stable below 150 K. When the pressure is increased up to 10 Torr, the adsorption is stable on Au(110)-(1  $\times$  2) up to a temperature of 350 K (cf. Figure 3b). For a fixed temperature of 300 K (cf. Figure 3c), the minimal pressure for adsorption on Au(110)-(1  $\times$  2) is between 1 and 10 Torr according to our thermodynamic approach. These results are in qualitative agreement with the high pressure RAIRS spectra of Y. Jugnet et al.<sup>9</sup> measured at room temperature, where the authors have shown that, below 10<sup>−3</sup> Torr, the CO intensity is zero. Going now to a lower temperature (100 K) (cf. Figure 3d), the calculations clearly indicate that CO adsorption is stable under UHV conditions. Adsorption structures on Au(230) are significantly less stable in the surface free energy diagram. Indeed, the energy gain resulting from the adsorption is not

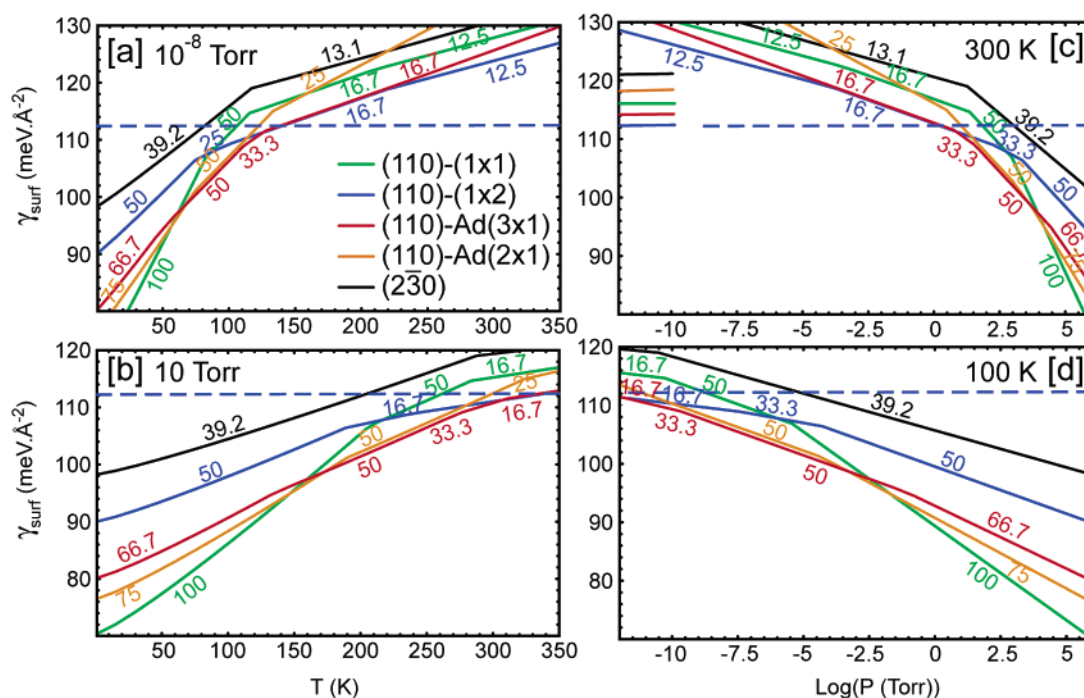


**Figure 3.** Surface free energy diagrams plotted (a) at  $10^{-8}$  Torr, (b) at 10 Torr, (c) at 300 K, and (d) at 100 K. For each surface, the evolution of the CO coverage (%) is reported. The surface energies of the clean surfaces appear in part c. The surface energy of the most stable clean surface Au(110)-(1  $\times$  2) is reported with horizontal dotted lines in all of the parts.

sufficient to balance the energy cost for forming such a stepped surface which present small terraces.

According to our thermodynamical results, the change of the temperature and pressure conditions unveils the existence of three different domains. The low coverage regime is always linked to a mixed adsorption phase on the ridge of Au(110)-(1  $\times$  2) and on a gold adatom located in the missing row. The medium coverage situation is systematically associated with coadsorption structures on the ridge of Au(110)-(1  $\times$  2) and on Au adatoms. In contrast, the saturation phase corresponds to CO adsorption on the non-reconstructed Au(110)-(1  $\times$  1) surface.

**C. Stretching Frequency Analysis.** The gas-phase CO molecule has been optimized in a large supercell of  $10 \times 10 \times 10 \text{ \AA}^3$  (cf. Table 2). The optimized C–O distance (1.142  $\text{\AA}$ ) is significantly longer than the experimental value (1.128  $\text{\AA}$ ), leading to a softer  $\nu(\text{CO})$  anharmonic stretching frequency (2106 vs 2143  $\text{cm}^{-1}$ ). This weakening of the vibration is the smallest one which has been calculated testing different pseudopotentials and GGA functionals. However, it is sufficiently strong ( $-37 \text{ cm}^{-1}$ ) to generate an equivalent systematic shift for the calculated frequencies of the adsorbed state. This error is compensated by the use of a scaling factor which is defined both at the harmonic and anharmonic levels (1.017) by dividing the experimental value (2143  $\text{cm}^{-1}$ ) by our corresponding DFT calculated stretching frequency (2106  $\text{cm}^{-1}$ ).

On the unreconstructed surface Au(110)-(1  $\times$  1), the scaled harmonic and anharmonic stretching frequencies are reported in Table 3, for various coverages. To compare the deviation between the calculated results and experiment, the frequency variation differences are also indicated in the table:

$$\Delta\tilde{\nu} = (\tilde{\nu}_{\text{ads}}^{\text{DFT}} - \tilde{\nu}_{\text{gas}}^{\text{DFT}}) - (\tilde{\nu}_{\text{ads}}^{\text{expt}} - \tilde{\nu}_{\text{gas}}^{\text{expt}}) \quad (5)$$

In the previous equation, the experimental references for the adsorbed phase and the gas phase are respectively 2110<sup>9</sup> and 2143  $\text{cm}^{-1}$  for all the surfaces. The frequency variation

differences are calculated at both the scaled harmonic and anharmonic levels. When the coverage changes from 12.5% up to 50%, the scaled anharmonic frequency does not vary significantly (2075–2079  $\text{cm}^{-1}$ ). These calculated frequencies are slightly harder than the one published recently, 2042  $\text{cm}^{-1}$ , by Shubina et al.<sup>27</sup> Our results correspond to a significant deviation from the RAIRS spectra obtained on Au(110)-(1  $\times$  2) (from  $-30$  to  $-34 \text{ cm}^{-1}$ ). Thus, the vibrational analysis supports the thermodynamic results showing that CO adsorption on Au(110)-(1  $\times$  1) should not be observed experimentally in the considered pressure range.<sup>9</sup> In contrast, at saturation coverage, the anharmonic frequency is red shifted up to 2092  $\text{cm}^{-1}$ . This high coverage value provides a much smaller deviation from experiment ( $-17 \text{ cm}^{-1}$ ). However, according to thermodynamics, this coverage should not be reached in the pressure range considered in the RAIRS experiments. For the adsorption on the missing-row reconstructed surface Au(110)-(1  $\times$  2), the scaled anharmonic frequencies vary slightly with the coverage (2070–2079  $\text{cm}^{-1}$ , cf. Table 4). The corresponding deviations from RAIRS measurements are also non-negligible (from  $-30$  to  $-39 \text{ cm}^{-1}$ ).

Coupling top CO adsorbates located on the ridges and on the adatoms generates more complex normal stretching modes from vibrational coupling (cf. Figure 4 and Figure 1d,e). In the case of the (3  $\times$  1)-2CO (33.3%) structure (occupation of sites A + B in Figure 1d), the infrared active mode ( $\nu_1$ ) at 2106  $\text{cm}^{-1}$  corresponds to an in-phase vibration of the top CO molecules adsorbed on the ridge and on the Au adatom of the cell (cf. Figure 5). In the second normal mode of the structure ( $\nu_2$ ) (2074  $\text{cm}^{-1}$ ), there is an out-of-phase vibration of the CO stretches. For the (3  $\times$  1)-3CO (50%) structure (cf. A + B + C in Figure 1d), three normal modes are obtained. The infrared active mode ( $\nu_1$ ) at 2107  $\text{cm}^{-1}$  is also associated with a complete in-phase vibration of the three top COs. The nonactive second mode ( $\nu_2$ ) at 2066  $\text{cm}^{-1}$  corresponds to an in-phase vibration of the top COs adsorbed on the ridge of the surface and an out-of-phase vibration of the Au–CO species. Finally, in the



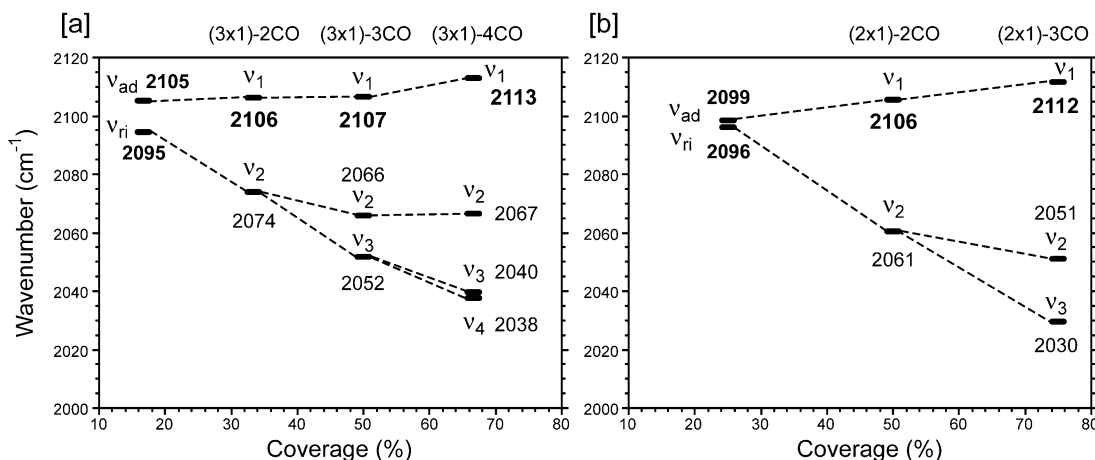


**Figure 4.** Evolution of the scaled harmonic stretching frequency as a function of CO coverage for the adsorption on the Au(110)-(1 × 2) surface presenting a Au adatom in the empty missing row with (a) a (3 × 1) periodicity (cf. Figure 1d) and (b) a (2 × 1) periodicity (cf. Figure 1e). The frequencies of the (3 × 1)-1CO (CO adsorbed on a ridge, cf. Figure 1c) and (3 × 1)Ad-1CO (CO adsorbed on a Au adatom, cf. A in Figure 1d) structures are also reported ( $\nu_{ri}$  and  $\nu_{ad}$ , respectively). For the structures having more than one normal mode, only the highest frequency modes ( $\nu_1$ ) are infrared active and appear in bold characters.

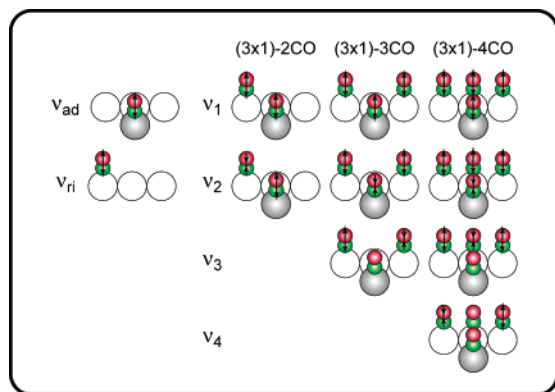


**Figure 5.** Stretching normal modes of the (3 × 1) adsorption structure where the CO molecules adsorb on the ridge of the missing row and on the Au adatom along the missing row (cf. Figure 1d).

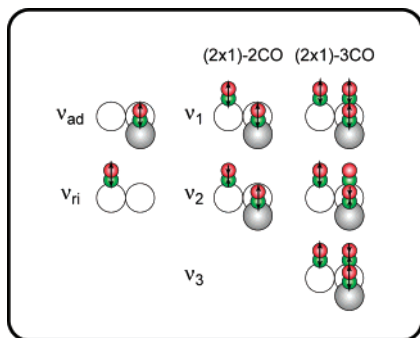


**Figure 6.** Stretching normal modes of the (2 × 1) adsorption structure where the CO molecules adsorb on the ridge of the missing row and on the Au adatom along the missing row (cf. Figure 1e).

nonactive third mode ( $\nu_3$ ) at 2052  $\text{cm}^{-1}$ , the top COs on the ridge vibrate antisymmetrically whereas the weight of the mode is zero on Au-CO. For the (2 × 1)-2CO (50%) structure (cf. A + B in Figure 1e), the normal modes are formed in a similar way (cf. Figure 6). When the coverage increases (from 16.67 to 66.67% for the (3 × 1) structure and from 25 to 75% for the (2 × 1) structure), the highest frequency associated with the active mode is slightly red shifted continuously from 2095 to 2105 and up to 2113  $\text{cm}^{-1}$  for the (3 × 1) structures, and from 2096 to 2099 and up to 2112  $\text{cm}^{-1}$  for the (2 × 1) structures.

Hence the coupling between the CO stretches of the adsorbates located on the ridge and the adatoms is weak.

In the works of Jugnet et al.,<sup>9</sup> the temperature is 300 K and the pressure varies from  $10^{-1}$  to  $10^2$  Torr. According to our thermodynamic model (cf. Figure 3c), five phases of Au(110)-(1 × 2) are stable competitively in that pressure range, with four of them involving the presence of Au adatoms in the empty troughs: (3 × 1)-1CO (16.7%) (cf. Figure 1c), (3 × 1)-1CO (16.7%) (cf. A in Figure 1d), (3 × 1)-2CO (33.3%) (cf. Figure 1d), (3 × 1)-3CO (50%) (cf. Figure 1d), and (2 × 1)-2CO (50%) (cf. Figure 1e). These adsorption structures are associated respectively with the scaled harmonic stretching modes at 2095, 2105, 2106, 2107, and 2106  $\text{cm}^{-1}$  (cf. Figure 4a,b). For the structures presenting more than one CO adsorbate, only the highest frequency mode is found to be infrared active. Since all these calculated frequencies are located in a narrow frequency window (the mean value being 2104  $\text{cm}^{-1}$ ), they can all be compared to the observed peak at 2110  $\text{cm}^{-1}$ . The major consequence of this result is that the presence of Au-CO species on the missing-row reconstructed surface is completely consistent with both thermodynamical and vibrational analyses. The calculations allow one to assign the observed band at 2110  $\text{cm}^{-1}$  to top CO adsorption both on the ridge of Au(110)-(1 × 2) and on Au adatoms present in the empty trough. The mean scaled harmonic frequency 2104  $\text{cm}^{-1}$  should also be compared to the IRAS measurements of Meier et al.<sup>26</sup> (2108–2118  $\text{cm}^{-1}$ ), since the coadsorption phases with Au-CO species are also competitive for a CO pressure of  $10^{-8}$  Torr in the temperature range 110–170 K, according to our thermodynamic results (cf. Figure 3a).

For the adsorption on the stepped Au( $\bar{2}30$ ) surface, the calculated frequencies are presented in Table 5. The values do not vary significantly with the coverage (2077  $\text{cm}^{-1}$ ), leading to a deviation from experiments of  $-32 \text{ cm}^{-1}$ . Hence, the adsorption along the steps of Au( $\bar{2}30$ ) is related to a CO stretch, not really different from the results obtained on Au(110).

#### IV. Conclusion

A detailed comparative study is reported for the CO adsorption on various Au surfaces. Total energy calculations are connected with atomistic thermodynamics to estimate the stability of the adsorption structures in the high pressure, high temperature conditions of the experiments. In addition, the CO

vibrational analysis is addressed for comparison with the measured RAIRS spectra. On all the surfaces, the top site is the most favorable one. The thermodynamical results show that two types of CO adsorption structures are competitive under the UHV conditions (low pressure and temperature) but also in the high pressure regime (up to 100 Torr) at room temperature. The first structure type is CO adsorption along the ridges of the missing-row reconstructed surface at various coverages, and the second one is a coadsorption structure where CO adsorbs both along the ridges of the reconstruction and on gold adatoms that are located in the empty troughs. The unexpected stability of the adsorption on gold adatoms has been explained by a stronger adsorption energy which compensates the energetic cost of the formation of such a surface defect. The coexistence of these structures is fully consistent with the vibrational analysis of the CO stretching frequency. The calculated vibrations show that the CO stretch is weakly sensitive to the surface reconstruction (missing row, adatom, step) and to the coverage. The high coverage situation is however associated with a small red shift of the CO frequency ( $10\text{ cm}^{-1}$ ). Hence, the experimental bands measured on Au(110)-(1 × 2) have been assigned to either a top CO adsorption located on the ridge of the surface or a coadsorption structure of top adsorbates located along the ridge and on gold adatoms present in the channels of the reconstruction.

**Acknowledgment.** The authors acknowledge Laurent Piccolo (Institut de Recherches sur la Catalyse, UPR CNRS 5401, France) for helpful discussions. They thank also the Institut du Développement et des Ressources en Informatique Scientifique (IDRIS) at Orsay (France), project 609, and the Centre Informatique National de l'Enseignement Supérieur (CINES) at Montpellier (France) for CPU time and assistance. They also thank the GdR Dynamique Moléculaire Quantique Appliquée à la Catalyse, a joint project of CNRS, Technische Universität Wien, and Institut Français du Pétrole. The CNRS-DFG bilateral project is also acknowledged for financial support.

## References and Notes

- (1) Haruta, M.; Kobayashi, T.; Sano, H.; Yamada, N. *Chem. Lett.* **1987**, 2, 405.
- (2) Haruta, M. *Catal. Today* **1997**, 36, 153.
- (3) Haruta, M.; Date, M. *Appl. Catal., A* **2001**, 222, 427.
- (4) Bond, G.; Thompson, D. *Catal. Rev.—Sci. Eng.* **1999**, 41, 319.
- (5) Bond, G.; Thompson, D. *Gold Bull.* **2000**, 33, 41.
- (6) Haruta, M.; Yamada, N.; Kobayashi, T.; Iijima, S. *J. Catal.* **1989**, 115, 301.
- (7) Schubert, M. M.; Plzak, V.; Garcke, J.; Behm, R. *J. Catal. Lett.* **2001**, 76, 143.
- (8) Haruta, M. *CatTech* **2002**, 6, 102.
- (9) Jugnet, Y.; Aires, F. J. C. S.; Deranlot, C.; Piccolo, L.; Bertolini, J. C. *Surf. Sci.* **2002**, 521, L639.
- (10) Binning, G.; Rohrer, H.; Gerber, C.; Weibel, E. *Surf. Sci.* **1983**, 131, L379.
- (11) Moritz, W.; Wolf, D. *Surf. Sci.* **1985**, 163, L655.
- (12) Gritsch, T.; Coulman, D.; Behm, R. J.; Ertl, G. *Surf. Sci.* **1991**, 257, 297.
- (13) Gimzewski, J. K.; Berndt, R.; Schlittler, B. R. *Phys. Rev. B* **1992**, 45, 6844.
- (14) Doyen, G.; Drakova, D.; Barth, J. V.; Schuster, R.; Gritsch, T.; Behm, R. J.; Ertl, G. *Phys. Rev. B* **1993**, 48, 1738.
- (15) Sturmat, M.; Koch, R.; Rieder, K. H. *Phys. Rev. Lett.* **1996**, 77, 5071.
- (16) Koch, R.; Sturmat, M.; Schulz, J. J. *Surf. Sci.* **2000**, 454–456, 543.
- (17) Outka, D. A.; Madix, R. J. *Surf. Sci.* **1987**, 179, 351.
- (18) Ruggiero, C.; Hollins, P. J. *Chem. Soc., Faraday Trans.* **1996**, 92, 4829.
- (19) Ruggiero, C.; Hollins, P. *Surf. Sci.* **1997**, 377–379, 583.
- (20) Gottfried, J. M.; Schmidt, J. J.; Schroeder, S. L. M.; Christmann, K. *Surf. Sci.* **2003**, 536, 206.
- (21) Goodman, D. W. *Chem. Rev.* **1995**, 95, 523.
- (22) Goodman, D. W. *J. Phys. Chem.* **1996**, 100, 13090.
- (23) Jensen, J. A.; Rider, K. B.; Salmeron, M.; Somorjai, G. A. *Phys. Rev. Lett.* **1998**, 80, 1228.
- (24) Somorjai, G. A.; Rupprechter, G. J. *Phys. Chem. B* **1999**, 103, 1623.
- (25) Osenzoy, E.; Meier, D. C.; Goodman, D. W. *J. Phys. Chem. B* **2002**, 106, 9367.
- (26) Meier, D. C.; Bukhtiyarov, V.; Goodman, D. W. *J. Phys. Chem. B* **2003**, 107, 12668.
- (27) Shubina, T. E.; Hartnig, C.; Koper, M. T. M. *Phys. Chem. Chem. Phys.* **2004**, 6, 4215.
- (28) Hammer, B.; Morikawa, Y.; Norskov, J. K. *Phys. Rev. Lett.* **1996**, 76, 2141.
- (29) Mavrikakis, M.; Stoltze, P.; Norskov, J. K. *Catal. Lett.* **2000**, 64, 101.
- (30) Liu, Z.-P.; Hu, P.; Alavi, A. J. *Am. Chem. Soc.* **2002**, 124, 14770.
- (31) Kandoi, S.; Gokhale, A. A.; Grabow, L. C.; Dumesic, J. A.; Mavrikakis, M. *Catal. Lett.* **2004**, 93, 93.
- (32) Molina, L. M.; Hammer, B. *Phys. Rev. Lett.* **2003**, 90, 206102.
- (33) Molina, L. M.; Hammer, B. *Phys. Rev. B* **2004**, 69, 155424.
- (34) Kresse, G.; Hafner, J. *Phys. Rev. B* **1993**, 47, 558.
- (35) Kresse, G.; Furthmüller, J. *Phys. Rev. B* **1996**, 54, 11169.
- (36) Perdew, J.; Wang, Y. *Phys. Rev. B* **1992**, 45, 13244.
- (37) Blöchl, P. *Phys. Rev. B* **1994**, 50, 17953.
- (38) Kresse, G.; Joubert, D. *Phys. Rev. B* **1999**, 59, 1758.
- (39) Monkhorst, H.; Pack, J. *Phys. Rev. B* **1976**, 13, 5188.
- (40) Makov, G.; Payne, M. *Phys. Rev. B* **1994**, 51, 4014.
- (41) Neugebauer, J.; Scheffler, M. *Phys. Rev. B* **1992**, 46, 16067.
- (42) Atkins, P. W.; Friedman, R. S. *Molecular Quantum Mechanics*, 3rd ed.; Oxford University Press: Oxford, U.K., 1997.
- (43) Kaxiras, E.; Bar-Yam, Y.; Joannopoulos, J. D.; Pandey, K. C. *Phys. Rev. B* **1987**, 35, 9625.
- (44) Qian, G.-X.; Martin, R. M.; Chadi, D. J. *Phys. Rev. B* **1988**, 38, 7649.
- (45) Reuter, K.; Scheffler, M. *Phys. Rev. B* **2003**, 68, 045407.
- (46) Reuter, K.; Scheffler, M. *Phys. Rev. B* **2001**, 65, 035406.
- (47) Höfner, C.; Rabelais, J. W. *Surf. Sci.* **1998**, 400, 189.
- (48) Ho, K. M.; Bohnen, K. P. *Europhys. Lett.* **1987**, 4, 345.
- (49) Yamagishi, T.; Takahashi, K.; Onzawa, T. *Surf. Sci.* **2000**, 445, 18.
- (50) Todd, B. D.; Lynden-Bell, R. M. *Surf. Sci.* **1993**, 281, 191.
- (51) Cox, H.; Liu, X.; Murrell, J. N. *Mol. Phys.* **1998**, 93, 921.
- (52) Möller, J.; Snowdon, K. L.; Heiland, W.; Niehus, H. *Surf. Sci.* **1986**, 178, 475.
- (53) Copel, M.; Gustafsson, T. *Phys. Rev. Lett.* **1986**, 57, 723.
- (54) Vlieg, E.; Robinson, I. K.; Kern, K. *Surf. Sci.* **1990**, 233, 248.
- (55) Ho, K.-M.; Bohnen, K. P. *Phys. Rev. Lett.* **1987**, 59, 1833.
- (56) Lozovoi, A. Y.; Alavi, A. *Phys. Rev. B* **2003**, 68, 245416.
- (57) Hammer, B.; Hansen, L. B.; Norskov, J. K. *Phys. Rev. B* **1999**, 59, 7413.
- (58) For the Au(110)-(1 × 1) surface, the following k-point densities have been chosen respectively for the (1 × 1), (2 × 1), (1 × 2), c(2 × 2), (2 × 2), (3 × 2), and (4 × 2) structures: 11 × 13 × 1, 7 × 13 × 1, 11 × 11 × 1, 9 × 9 × 1, 5 × 9 × 1, 5 × 5 × 1, and 5 × 3 × 1. For the Au(110)-(1 × 2) surface, the k-point meshes are respectively for the (1 × 1), (2 × 1), (3 × 1), and (4 × 1) structures the following: 7 × 13 × 1, 5 × 9 × 1, 5 × 5 × 1, and 5 × 3 × 1. For the Au(230) surface, a tight convergence is reached with the following k-point densities for the (1 × 1), (2 × 1), and (3 × 1) structures, respectively: 8 × 5 × 1, 5 × 5 × 1, and 4 × 4 × 1.